A new super resolution and deblurring algorithm for Magnetic Resonance images based on sparse representation and dictionary learning

Sanaz Sahebkheir[1], Ali Esmaeily[2]*, Mohammad Saba[3]

[1] M.Sc. in Remote Sensing Engineering, Department of Surveying Engineering, Graduate University of Advanced Technology, Kerman, Iran

[2] Department of Surveying Engineering, Graduate University of Advanced Technology, Kerman, Iran

[3] Department of Radiology, Medical Science University, Kerman, Iran

ABSTRACT

Magnetic Resonance Imaging (MRI) provides a non-invasive manner to aid clinical diagnosis, while its limitation is the slow scanning speed. Recently, due to the high costs of health care and taking account of patient comfort, some methods such as Parallel MRI (pMRI) and compressed sensing MRI have been developed to reduce the MR scanning duration under the sampling process. It is almost unavoidable to accept some doses of X-rays in computed tomography (CT scans). If one could find a more efficient way to represent the required visual information, the tasks of image processing and medical imaging would become easier and less troublesome. In this paper, first, we used pMRI on complex double data of brain magnetic resonance image. pMRI significantly reduces the number of measurements in the Fourier domain because each coil only acquires a small fraction of the whole measurements. It is important to reconstruct the original MR image efficiently and precisely for better diagnosis. In this research, we proposed a new super resolution and deblurring algorithm with dictionary learning, based on assuming a local Sparse-Land model on image patches, serving as regularization, then we validated the proposed method by using another one called the adaptive selection of sub dictionaries- adaptive reweighted sparsity regularization. Visual comparison and significant difference in psnr calculation (0.8111db) and time complexity showed that the proposed method had much better results.

1. Introduction

In medical imaging, such as magnetic resonance imaging (MRI), patients have to stay in the machine for more than 30 minutes for a scan of the major parts. In order to obtain a high-quality image, it is almost unavoidable to accept some doses of X-rays in computed tomography CT scans (Lee et al., 2004). Finding a better way of representing visual information with scan time reduction included will benefit patients and health care economics. Local motions, e.g. breathing and heart beating during long time scanning, may result in ghosting, smearing, streaking on the reconstructed MR image (Chen et al., 2013). Many applications such as medical image processing, require resolution enhancement of images acquired by low-resolution sensors (e.g., for high-resolution displays) while minimizing visual artifacts (Zeyde et al., 2011).

The hydrogen nuclei in a patient, often just referred to as protons, behave like tiny bar magnets. Hydrogen makes up 80% of all atoms found in the human body, making hydrogen extremely useful for MRI. Because hydrogen is a single charged spinning nucleon, the hydrogen nucleon exhibits magnetism due to its angular momentum and magnetic moment; before the patient is put into the B0 magnetic field, the magnetic moments of the patient's nuclei are randomly oriented. Under normal circumstances, magnetic dipoles (each has a north and south magnetic pole) are randomly

distributed in space. Consequently, if the net magnetic field of a patient was measured, it would be zero because all of the individual magnetic dipole moments were canceled (Carlyle et al., 2015). Most of the information in the natural images are redundant (Marial et al., 2014). Human eyes can quickly obtain key information of an image without looking at the details of each pixel. Our interesting data pieces are relatively very sparse compared with the whole data. Most MR images are sparse in an appropriate transform domain. More complex imagery, such as brain images, can be sparsified in more sophisticated domains, such as the wavelet domain (Lustig & Pauly, 2010).

The MR image reconstruction process can be formulated as:

$$x = \arg\min_{x} \left\{ \frac{1}{2} \|Fx - b\|^2 + \alpha \|x\|_{TV} + \beta \|\phi x\|_1 \right\} \qquad (1)$$

Where x is an MR image to be reconstructed, F is the under-sampled Fourier transform, b is the vector of k-space measurements, ϕ is the wavelet basis, $\|x\|_{TV}$ is the total variation defined as:

$$\|x\|_{TV} = \sum_{i=1}^{N} \sqrt{((\nabla_1 x_i)^2 + (\nabla_2 x_i)^2)} \qquad (2)$$

Here, ∇_1 and ∇_2 denote the forward finite difference operators on the first and second coordinates. α and β are two parameters to be tuned.

Sparsity based techniques have shown great success in medical image processing. They are also very useful in image processing and computer vision, such as image registration (Peng et al., 2010), face recognition (Wright et al., 2009), image super resolution (Yang et al., 2010), background subtraction (Huang et al., 2009), photometric stereo (Reddy et al., 2009), etc. The ability of sparse representations to uncover semantic information in image processing and computer vision is based on the fact that the images (naturally very high dimensional) often lie on or near low dimensional subspaces, sub-manifolds, or stratifications (Wright et al., 2010). The optimization methods such as L_1 norm minimization can efficiently extract such key structures, and then recover the original image without or with little information loss. The algorithms that are based on sparse representation can often achieve state-of-the-art performance if sparsity is appropriately applied (Wright et al., 2010). In medical image processing, sparsity is used for solving problems in a lot of practical issues. The sparsity patterns are not randomly distributed but follow some special structures. For example, in diffuse optical imaging (Chen et al., 2014), the activation area of the human brain corresponding to a finger tapping task often is sparse among the whole brain. In addition, such activation is often clustered in a certain region. In dynamic MR images (Li et al., 2014),

all the images of a cardiac motion have very similar structures along the temporal direction. In background subtraction (Peng et al., 2014), the foreground objects often consist of mutually connected pixels but not randomly distributed ones. Theoretically, it has been shown that better performance can be obtained if more prior information about the data is exploited (Huang, 2011). Many of the existing algorithms may not be efficiently able to solve complex sparsity inducing problems. This issue motivated the authors to develop a new efficient method for super-resolution and deblurring of complex data such as MRI images. We used sparse prior, for the first time, and assumed that if the reconstructed image using pMRI still possesses blurs, deblurring it will form the highest resolution.

2. Related Works

Resolution (consequently, the quality of given images) is more than a traditional image processing term (Ferreira., 2016). Single image super-resolution (SR) can be classified into three categories: Interpolation-based, Reconstruction-based and Example learning-based. Zhang et al. (2006) utilized the correlation between pixels to construct a prediction function to estimate the missing pixel. Zhu et al. (2014) proposed a fast single image super-resolution method that combines self-example learning and sparse representation by replacing the exact SVD[1] and L_1 norm with K-SVD and L_0 norm to achieve rapid self-learning. Dong et al. (2013) proposed nonlocal similarity, a critical type of self-similarity, which is incorporated into the sparse representation model to constrain and improve the estimation of sparse coefficients

To add more diversified and abundant patterns to the internal dictionary, Huang et al. (2015) proposed to expand the internal patch search space by localizing planes with detected perspective geometry variations in the LR[2] image. Some external SR[3] methods apply the learned priors to SR estimation directly, without any online auxiliary adaptation; thus they are categorized into fixed external methods, including neighbor embedding (Timofte et al., 2014), kernel ridge regression (Kim et al., 2010), factor graph (Xiong et al., 2013), kernel PCA (Chakrabarti et al., 2007), locality-constrained representation (Jiang et al., 2014), and coupled dictionary (He et al., 2013). Several methods have been developed for super-resolution based medical image analysis, including sparse representation based MR spectroscopy quantification, constrained generative regression model-based Fmri[4] analysis, filter-based machine intelligence, sparse coding based super-resolution learning, similar based image blocks sparse relation (Li et al., 2017). Huang et al. (2018) used an algorithm based on an improved

---

[1] Singular value decomposition
[2] Low resolution

[3] Super Resolution
[4] Functional Magnetic Resonance Imaging

sparse autoencoder for image super-resolution, and the result showed that the proposed SRISAE algorithm achieved significant improvement in terms of both quantitative and qualitative measurements.

3. Reconstructing image with pMRI based on compressed sensing SENSE

The data acquisition step in conventional MRI is a relatively slow sampling procedure. To improve the scanning speed of MRI, an efficient and feasible way is to acquire the data in parallel with multi-channel coils. The scanning time depends on the number of measurements in the Fourier domain, and it will be significantly reduced when each coil only acquires a small fraction of the whole measurements. In literature, this issue is called pMRI. By surrounding the scanned objects by an array of multiple sensing coils, pMRI can extract spatial information from many coils in parallel, resulting in accelerated data acquisition. Such pMRI techniques use spatial information from arrays of RF detector coils to substitute the phase encoding that would otherwise have to be obtained in a sequential fashion using field gradients and RF pulses. The use of multiple effective detectors has proved to multiply the imaging speed, without increasing gradient switching rates or RF power deposition. For Fourier pulse sequences that sample a rectilinear trajectory in k-space, parallel imaging techniques invariably reduce the number of phase encoding steps needed to sample k-space and thereby reduce the imaging time.

The coil sensitivity information is used during the image reconstruction to remedy the loss of spatial information. Parallel imaging techniques are classified into one of two categories. They can fill in the omitted k-space lines prior to Fourier transformation, by constructing a weighted combination of neighboring lines obtained by different RF detector coils (Glowinski et al., 2016). They can first Fourier transform the under-sampled k-space dataset to produce an aliased image from each coil, and then unfold the aliased signals by a linear transformation of the superimposed pixel values. Two such parallel imaging techniques that have recently been developed and applied to vivo imaging are SENSE (Sensitivity Encoding) and SMASH (simultaneous acquisition of spatial harmonics) (Glowinski et al., 2016).

Sparsity techniques have been used to improve the classical method SENSE (Pruessmann et al., 1999). Unlike previous CS SENSE (Liang et al., 2009), which reconstructs the images of multi coils individually, calibration of parallel MRI (Chen et al., 2013) recovers the aliased images of all coils jointly by assuming the data is jointly sparse.

There are two steps for compressed sensing pMRI reconstruction (Chen et al., 2013): 1) The aliased images are recovered from the under-sampled Fourier signals of different coil channels by CS[5] methods; 2) The final image for clinical diagnosis is synthesized by the recovered aliased images using the sum-of-square (SoS) approach. SENSE is based on the following acquisition model: for j=1...,J

$$RfS_j u = b_j + \eta$$, where u is the unknown image, b_j is the vector of measured partial Fourier coefficients at the jth receiver, R is a diagonal sub-sampling operator, f is the Fourier transform, η is the Gaussian noise, and J is the total number of coils. The operator S_j is a diagonal matrix sensitivity mapping for the jth receiver, as is used to compensate for the decay of signal intensity with distance from each pixel. Finally, the sensitivity map S_j can be estimated. The flowchart diagram of the Compressed Sensing SENSE in pMRI is represented in Figure1.

3.1. Calculating partial Fourier coefficients

Partial Fourier imaging techniques are the reconstruction methods in which the data from as little as one-half of k-space is used to generate an entire MR image. This result originates from the fact that some of the information in k-space is redundant. The provided phase-less errors occur during data collection, k-space possesses a peculiar mirrored property known as conjugate (or Hermitian) symmetry (McGibney et al., 1993). Conjugate symmetry applies to pairs of points (like P and Q) that are located diagonally from each other across the origin of k-space. If the data at P is the complex number [a+bi], the data at Q is immediately known to be P's complex conjugate, [a−bi] (LR, 2011). Conjugate symmetry can be shown to exist whenever a Fourier transform is performed on any real-valued function. In more concrete terms related to 2D MR imaging, the conjugate symmetric points represent corresponding data acquired on the rising and trailing tails of two echoes obtained with opposite phase encoding steps. In other words, the signal intensity of a point on the rising portion of an echo obtained using a positive phase-encode step is the complex conjugate of that signal on the downward portion of another echo obtained using the corresponding negative phase-encode step (Feinberg et al., 1986).

The practical result of conjugate symmetry is that only half of k-space data need to be collected and the other half can be estimated. This can be translated into a reduction in imaging time, reduction in minimum echo time, or both. Conjugate symmetry of P and Q is shown in Figure 2. In this paper, due to the fine reconstruction of pMRI, it was used on complex double data of brain magnetic resonance image downloaded from https://www.data.gov/ in .mat format. The result of pMRI is shown in Figure 10.

Also, pMRI reconstructs the data as well, but some blurs appear. To overcome this gap, we assume that by deblurring

---

[5] compressed sensing

and removing the blur from the image, the resulting image has the highest quality. Deblurring steps are as follows:

4. The Proposed super resolution and deblurring algorithm

Image restoration (IR) tries to reconstruct a high quality image x from its degraded version y, Which is a typical ill-posed inverse problem (Bertero et al., 1998). IR can be formulated as:

$$z_l = SHy_h + v \tag{3}$$

Where y is the unknown image to be estimated, H and S are degrading operators and v is the additive noise. Here the additive noise is a white Gaussian noise $v \square N(0, \sigma^2 I)$. When H and S are identities, the IR problem becomes denoising; when S is identity and H is a blurring operator, IR becomes deblurring; when S is identity and H is a set of random projections, IR becomes compressed sensing (Donoho, 2006). When S is a down-sampling operator and H is a blurring operator, IR becomes (single image) super-resolution. Due to the Gaussian nature of v, the maximum likelihood estimation is obtained to minimize $\|SHy_h - z_l\|_2$. Since SH has more columns than rows, it cannot be inverted stably; this leads to infinite solutions with zero values in the least-square term. In order to solve this problem, the sparse land model used (Zeyde et al., 2011). The super resolution problem is described in Figure 3. This model assumes that each patch of the image can be well represented by a linear combination of few dictionary atoms. The steps of the proposed method are shown in Figure 4. The steps of super resolution and deblurring algorithm are represented in sections 4.1 to 4.7. The test image here is the pMRI reconstruction result, in order to be deblurred.

4.1. Incorporating the sparse-land prior

In order to avoid dealing with the complexities of different resolutions between z_l and y_h, and simplifying the recovery algorithm, it is assumed that the image z_l is scaled-up by a simple interpolation operator $Q : R^{N_h} \rightarrow R^{N_l}$ (here Bicubic interpolation), which fills in the missing rows and columns, returning to the size of y_h. Therefore, computational complexity reduces subsequently. y_l denote as scaled-up image and calculated by the following equation:

$$Qz_l = Q(SHy_h + v) = QSHy_h + Qv = L^{all}y_h + \tilde{v} \tag{4}$$

The goal is to process $y_l \in R^{N_h}$ and produce $\hat{y}_h \in R^{N_h}$ as a result which is the closest high-resolution image to the original one, $y_h \in R^{N_h}$.

The algorithm operates on the patches extracted from y_l aiming to estimate the corresponding patches from y_h.

$P_h^k = R_k y_h \in R^N$ is a high-resolution image with a patch size of $\sqrt{n} \times \sqrt{n}$, extracted by the operator $R_k : R^{N_h} \rightarrow R^n$ from the image y_h in location k. $\{k\}$ location is centered around true pixels in the low-resolution image y_l.

$P_h^k \in R^n$ can be represented by $q^k \in R^m$ over the dictionary $A_h \in R^{n \times m}$, $P_h^k = A_h q^k$. A_h is the dictionary matrix containing high-resolution patches. $P_l^k = R_k y_l$ are corresponding low-resolution patches extracted from y_l in the same location (centered around the same pixel k with $\sqrt{n} \times \sqrt{n}$ patch size). The operator $L_{all} = QSH$ transforms the complete high-resolution image y_h to the low resolution y_l. L is a local operator being a portion of L_{all}. Low-resolution patch P_l^k can be represented by the same sparse vector q^k over the dictionary $A_l = LA_h$. The sparse representation vector q^k is found for P_l^k, then P_h^k can be resolved by multiplying the representation by the dictionary A_h. In order to focus on the resolution between the low-resolution patches and the edge and texture content corresponding to high-resolution ones, a high-pass filtering technique was employed directly on the full images. Local patches formed the dataset $P = \{P_h^k, P_l^k\}$. P_h^k patches with $\sqrt{n} \times \sqrt{n}$ pixel sizes are extracted from the high-resolution images e_h^j. The corresponding low-resolution P_l^k patches are extracted from the same locations in filtered images $f_k * y_l^j$ with the same size ($\sqrt{n} \times \sqrt{n}$ pixels). The high-resolution patch size should be at least $s \times s$ to cover the whole image and to improve the reconstruction result (by reducing errors and discontinuities between the reconstructed patches). Figure5 represents the flow diagram of the sparse-land prior

4.2. Image interpolation (Bicubic)

Bicubic interpolation is used to construct the unknown data points on the regular grids of a High-resolution image from known data points of a low-resolution image (Yang et al, 2010). Bicubic interpolation has a low computational cost and it over-smooths the image and creates edge halos. This method uses Bicubic interpolation to synthesize a low-resolution input image into its high-resolution version (Figure 6).
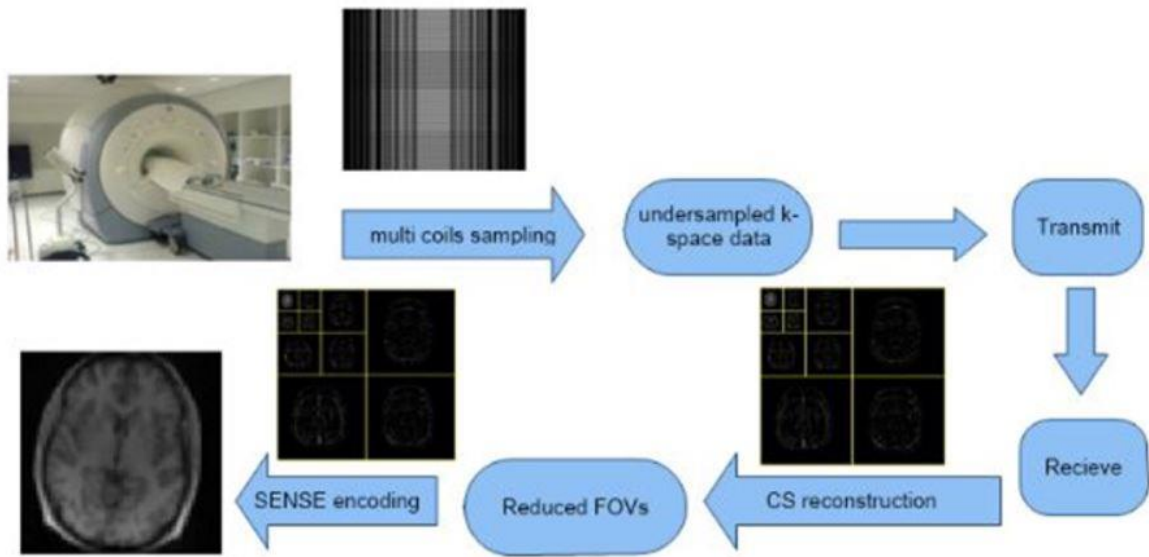
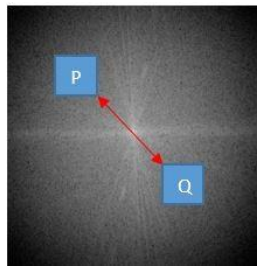Figure1. Flow diagram of the Compressed Sensing SENSE in pMRI

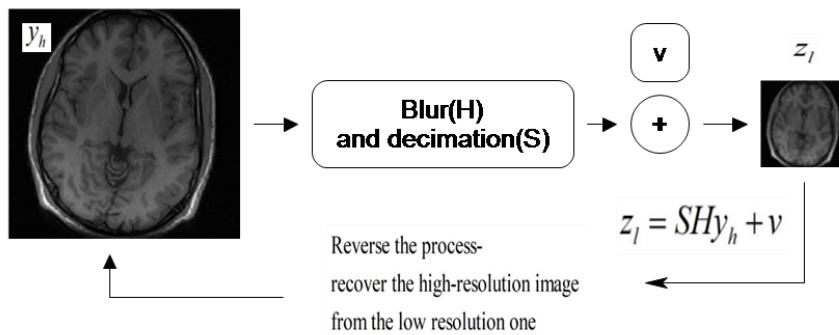Figure2. Conjugate symmetry of P and Q. If the data for one is known, the other one can be calculated

$$z_l = SHy_h + v$$

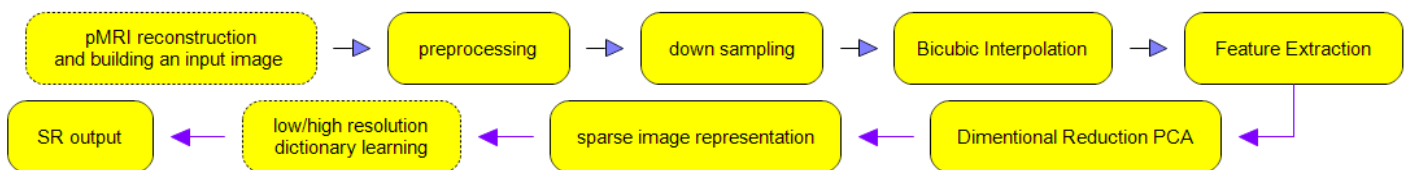Figure3. Illustrates the super resolution problem

Figure.4. Flow diagram of the proposed method

4.3. Training phase

a. Training set construction: A set of high-resolution training images $\{y_h^j\}_j$ are collected, Low-resolution images $\{y_l^j\}_j$ are constructed using the scale-down operator l_{all} and pairs of matching patches that form the training database $P=\{P_h^k, P_l^k\}_k$ are extracted.

b. Each of these patches-pairs undergo a pre-processing stage that removes the low-frequencies from P_h^k and extracts features from P_l^k

c. Dimensionality reduction is applied on the features of low-resolution patches P_l^k, making the dictionary training step much faster.

d. A dictionary A_l is trained for low-resolution patches so that they can be represented sparsely.

e. A corresponding dictionary A_h is constructed for high-resolution patches so that it matches the low-resolution one.

4.3.1. Reconstruction phase

a. Given a low-resolution image test z_l to be scaled-up, it is interpolated to y_l of the destination size, and it requires only spatial non-linear filtering to sharpen it.

b. Pre-processed patches P_l^k are extracted from each location $k \in \Omega$ and are then sparse coded using the trained dictionary A_l

c. The found representations $\{q^k\}$ are then used to recover the high-resolution patches by multiplying them with A_h to obtain approximated high-resolution patches.

d. The recovered high-resolution patches $\{P_h^k\}$ are finally merged by averaging in the overlap area to create the resulting image.

4.3.2 Training Set Construction

The training phase starts by collecting several images $\{y_h^j\}_j$ which are considered to be the high-resolution examples. Each of these images is blurred and down-scaled by a factor of s. This leads to the formation of the corresponding low-resolution images $\{Z_l^j\}_j$, which are then scaled up back to the original size using Q resulting with the set $\{y_l^j\}_j$ Thus, $y_l^j = L_{all}y_h^j + V$ .S,H and Q should be used in both training and reconstruction phases.

4.4. Preprocessing and feature extraction

Similar to the approach proposed by Wang et al. (2010), High-pass filtering is employed directly on the full images which avoided boundary problems due to the small patch size. High-resolution low-frequencies are removed by computing $e_h^j = y_h^j - y_l^j$. Typical filters to be used are gradient and Laplacian high-pass filters. After the two pre-processing steps described above, local patches are extracted, forming the data-set $P=\{P_h^k, P_l^k\}_k$ and patches of size $\sqrt{n} \times \sqrt{n}$ pixels are extracted from the high-resolution images e_h^j. The corresponding low-resolution P_l^k patches are extracted from the same locations in the filtered images $f_k * y_l^j$.

4.4.1. Dimensionality reduction

The formed low-resolution image patches start at n/s^2 dimensionality and it should not increase. The advantage of performing a dimensionality reduction is saving computations in the related training and super-resolution algorithms. Therefore, the last step before dictionary learning is dimensional reduction of the low-resolution image patches. In order to reach this goal, Principal Component Analysis (PCA) algorithm is implemented on the vectors.

4.5. Dictionary learning

Low-resolution dictionary $A_l \in R^{n_l \times m}$ constructed by applying K-SVD algorithm on low-resolution training patches $A_l \in R^{n_l \times m}$: A_l (Aharon, et al., 2006),

$$\{q^k\} = \arg\min_{A_l, \{q^k\}} \sum_k \|P_l^k - A_l q^k\|^2 \; s.t. \|q^k\|_0 \leq L \quad \forall k \quad (5)$$

The product of this step is sparse representation vectors $\{q^k\}_k$ corresponding to the training patches $\{P_l^k\}_k$. The next step is constructing the high-resolution dictionary. The purpose is to reconstruct P_h^k patches by approximation of $P_h^k \approx A_h q^k$. The high-resolution dictionary A_h is defined to be the one that minimizes the approximation error

$$A_h = \arg\min_{A_h} \sum_k \|P_h^k - A_h q^k\|_2^2 = \arg\min_{A_h} \|P_h - A_h Q\|_F^2 \quad (6)$$

Matrix P_h is constructed with high-resolution training patches $\{P_h^k\}$. The columns of Q are similar to the columns of $\{q^k\}$ (Wang et al., 2010).

4.6. Bootstrapping approach

The algorithm is able to bootstrap itself from a single test image as proposed by Glasner et al., (2009). Low-and high-resolution dictionaries $\{A_l, A_h\}$ can be trained with a pair of low and high-resolution images. The test image is considered as the high resolution image. The low resolution image will

be obtained using appropriate degrading factors (S and H). Here, image super-resolution was based on a bootstrapping approach and a sparse land model and a test image itself.

4.7. Summary of the algorithm

a. Constructing y_l using scale-down operator L_{all}

b. Pre-processing of y_l

c. Applying high pass filtering and down-sampling by a factor of $s=3$

d. Scaling up the image to original size followed by Bicubic interpolation

e. Feature extraction of patches with a size of $\sqrt{n} \times \sqrt{n}$ pixels in y_l Using Laplacian and gradient filters

f. Feature dimension reduction using PCA

g. Using the OMP[6] algorithm and allocating l atoms per patch presentation

h. High-resolution dictionary training using the pseudo-inverse expression $A_h = P_h Q^+$ and low-resolution dictionary training with K-SVD algorithm

l. Obtaining approximated high-resolution patches by multiplying the high-resolution dictionary and representation vectors.

The flowchart diagram of the super-resolution algorithm is depicted in Figure7.

5. Validation of experiment

The most important part of the super-resolution and deblurring algorithm is choosing the best dictionary for this purpose. Many dictionary learning methods applied to the result of pMRI but our proposed method had the best result so we choose one of the frequently used dictionary learning methods based on adaptive sparse domain selection and adaptive regularization (ASDS). We evaluated the proposed method with Bicubic interpolation and ASDS, ASDS-AR, ASDS-AR-NL methods. Two different dictionaries were used for reconstruction (introduced as TD1 and TD2) and implementation on the result of pMRI. Then, they were compared with psnr, time complexity and visual results.

5.1. Adaptive sparse domain selection and adaptive regularization

Sparse representation owes its success to the development of l_1-norm optimization techniques. Considering the fact that image content can vary significantly in a single image, various image patches were collected and the local sparse domain was adaptively selected. Two adaptive regularization terms were introduced into sparse representation. A set of autoregressive(AR) model learned from the chosen dataset.

The best fitted AR models are adaptively selected to regularize the local structures. The flowchart of the validation method is shown in Figure 8. The ASDS[7] is based on sparse representation with a union of dictionaries and local selection of trained sub-dictionaries. In addition to sparsity regularization, they proposed two more regularization terms: one that characterizes the local image structures, named Autoregressive Model (AR), and other one that preserves edge sharpness and suppressing noise, named Non-Local Self-Similarity Constraint (NL). All those terms served as a regularization term. ASDS uses the regularization terms AR and NL to obtain reasonable estimates of the sparse coding coefficients of the original image, and then centralizes the sparse coding coefficients of the observed image to those estimates. Moreover, the ASDS method is characterized by learning the sub-dictionaries offline and selecting the best sub-dictionary online. In this algorithm, the authors used the Iterative Shrinkage-thresholding (IST) algorithm to solve the l_1-minimization problem generated by the models (Ferreira, 2016). In the ASDS method $y=DHx$ is defined as an appropriate model, where y is the Low-Resolution image, x is the High-Resolution image, D is a down-sampling operator and H is a Gaussian kernel, y_i and x_i the Low- and High-Resolution patches, respectively, extracted from y and x using the operator R_i. Using the IST algorithm, where α is composed of all sparse vectors α_i, $\hat{x}$ is the estimation of x and $\hat{x}_i$ is the estimation of patches x_i. Using ASDS, the super-resolution problem is formulated as: $\hat{\alpha} = \arg\min_{\alpha} \left\{ \|y - DH\phi.\alpha\|_2^2 + \lambda\|\alpha\|_1 \right\}$. The IST algorithm that is used for the estimation of α is composed of all sparse vectors. The main procedure in ASDS is the determination of ϕ_{k_i} which best fitted to each local patch. The best sub-dictionary ϕ_{k_i} is selected and assigned to each x_i using

$$k_i = \min_k \left\| \phi_c \hat{x}_i^h - \phi_c \mu_k \right\|_2 \tag{7}$$

where ϕ_k are trained orthonormal sub-dictionaries, μ_k is the centroid of each cluster available and ϕ_c is a projection matrix that consists of the first several most significant eigenvector, and $\hat{x}_i^h$ is a high-pass filtered patch of $\hat{x}_i$.

Moreover, $\hat{x} = \phi.\alpha$ is defined as

$$\left(\sum_{i=1}^{N} R_i^T R_i \right)^{-1} \left(\sum_{i=1}^{N} R_i^T \phi_k^i \hat{\alpha}_i \right) \tag{8}$$

---

[6] Orthogonal Matching Pursuit

[7] Adaptive Sparse Domain Selection

where R_i is a matrix that extracts x_i. Then, the following problem

$$\hat{\alpha} = ar\min_{x} \left\{ \underbrace{\left\| y - DH\phi.\alpha \right\|_2^2}_{\text{first term}} + ... \right.$$

$$\underbrace{\gamma \left\| (I-A)\phi.\alpha \right\|_2^2}_{\text{second term}} + ...$$

$$\underbrace{\eta \left\| (I-B)\phi.\alpha \right\|_2^2}_{\text{third term}} + ... \qquad (9)$$

$$\left. \underbrace{\sum_{i=1}^{N} \sum_{j=1}^{n} \lambda_{i,j} \left| \alpha_{i,j} \right|}_{\text{fourth term}} \right\}$$

is solved iteratively to find the estimated $\hat{\alpha}$ using the IST algorithm subject to a stop criterion, where ϕ is the set of all sub-dictionaries $\{\phi_k\}$. $\alpha_{i,j}$ is a coefficient related to j^{th} atom of ϕ_{k_i} and $\lambda_{i,j}$ is dedicated weight to $\alpha_{i,j}$. $\lambda_{i,j}$ is empirically computed as $\lambda_{i,j} = 1 / \left(\left| \hat{\alpha}_{i,j} \right| + \varepsilon \right)$ where $\hat{\alpha}_{i,j}$ is the estimate of $\alpha_{i,j}$ and ε is a small constant. η is a constant balancing the contribution of non-local regularization, I is the identity matrix, α is an AR parameter vector, γ is a constant balancing the contribution of the AR regularization term.

Table 1 represents a description of the symbols used in this paper. In Equation (9), the first l_2-term is the reliability term, guaranteeing that the solution $\hat{x}$ can well fit the observation y after degradation by operators H and D. The second l_2-term is the local AR model-based adaptive regularization term, requiring that the estimated image is locally stationary. The third l_2-term is the non-local similarity NL regularization term, which uses the non-local redundancy to enhance each local patch. The last weighted l_1-norm, named here as the fourth term, is a sparsity penalty term, requiring that the estimated image should be sparse in the adaptively selected domain. The ASDS method initializes the training set D by extracting the patches from several natural training images that are rich in edges and texture in the scale space of the HR image. PCA was used for training the patches in D that were obtained from the K-means algorithm.

6. Results

In this section, we represent the results of the proposed method and its comparison obtained from Zhang et al., (2011). First, we used pMRI technique for reconstructing magnetic resonance imagery in complex double type downloaded from https://www.data.gov/. The reconstruction

[8]http://www.eecs.berkeley.edu/Research/Projects/CS/vision/grouping/segbench

procedure took about 3 minutes implemented in Matlab 2016b on a desktop Intel corei7 8550U CPU. The result of pMRI is shown in Figure 10. After the reconstruction, some blurs appeared; this time we assumed that by deblurring and removing the blurs, the image should be reconstructed in the best of its quality. The result of pMRI is the test image for the deblurring step. We studied several deblurring and super-resolution methods based on sparse representation modeling and dictionary learning to find the best dictionary. The proposed method for deblurring was implemented in the same environment using optimized K-SVD and OMP. High-resolution images were used for training data downloaded from the Berkeley segmentation database[8] (Figure 9). For the validation algorithm, we extended the training set by $90°$ rotation considering that the human visual system is sensitive to image edges. For fair comparison, the degraded factor (s=3) and white Gaussian noise with a standard deviation of 2 were adopted for both algorithms. In the proposed method, the training image was blurred with bicubic filter and then degraded with an s factor of 3. Feature extraction was conducted by Laplacian filters and gradient, for which nearly bout 130,000 training patch pairs were gathered, and with the PCA feature, the dimension reduced to 30. The dictionary learned for low-resolution images with 40 iterations of the K-SVD algorithm with 1000 atoms in the dictionary and allocating 3 atoms to each patch representation which took about 10 minutes on the same environment. Learning the dictionary for high-resolution images with pseudo-inverse expression $A_h = P_h Q^+$, took only 45 seconds. By running the whole algorithm, the high-resolution image was reconstructed in 30 seconds. The dictionary learning procedure for validation algorithm took 12 hours and the deblurring process took about 5 minutes for 700 to 1000 iterations. This suggests that the proposed algorithm is much faster. Choosing the right patch size is very important. In the proposed method, larger patch sizes result in overlaps between the patches, which improve the reconstruction result (by reducing errors and discontinuities between reconstructed patches). In the validation algorithm, we used various patch sizes (3×3 or 5×5 or 7×7). The results show that small patch sizes (3×3 or 5×5) tend to generate artifacts in smooth parts, and the reconstructed edges are not sharp enough. For validating the algorithm by choosing a 7×7 patch size, 727,615 patches were extracted from the training images.

As a cluster-based method, choosing the number of classes is very important. Small classes tend to smooth class boundaries. Large-number classes, however, make sub-dictionary less reliable.Therefore, we chose 200 clusters containing less than 300 patches. The psnr (peak of snr) calculated by Eq. (10):

Extraction of patch from y_h in location k performed by

$$P_k^h = R_k y_y$$

Model Assumption: Every such patch can be represented sparsely over the dictionary A_h

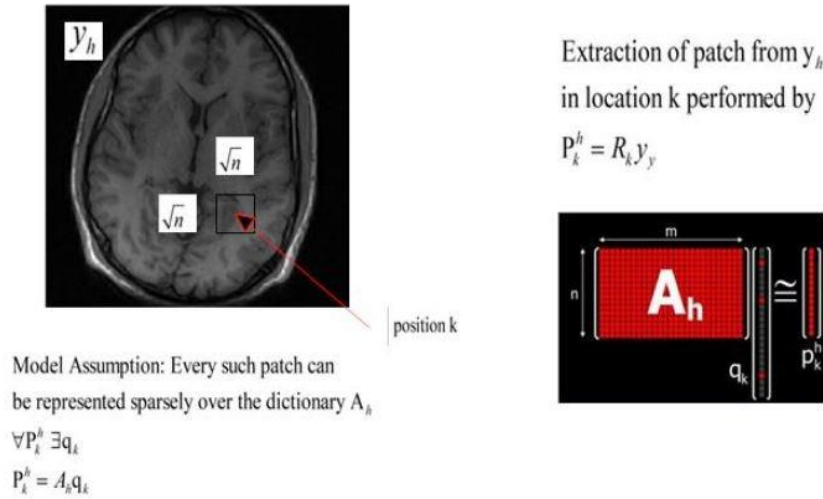$$\forall P_k^h \; \exists q_k$$
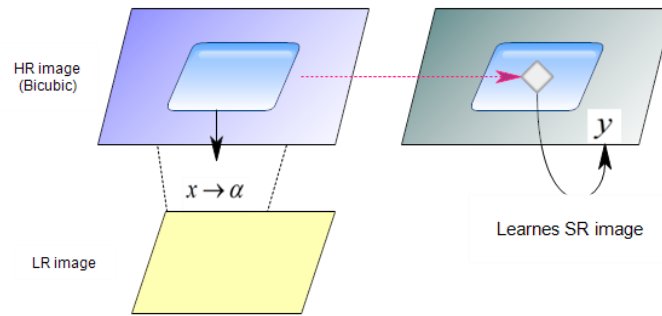
$$P_k^h = A_h q_k$$

Figure 5. Sparse-land prior

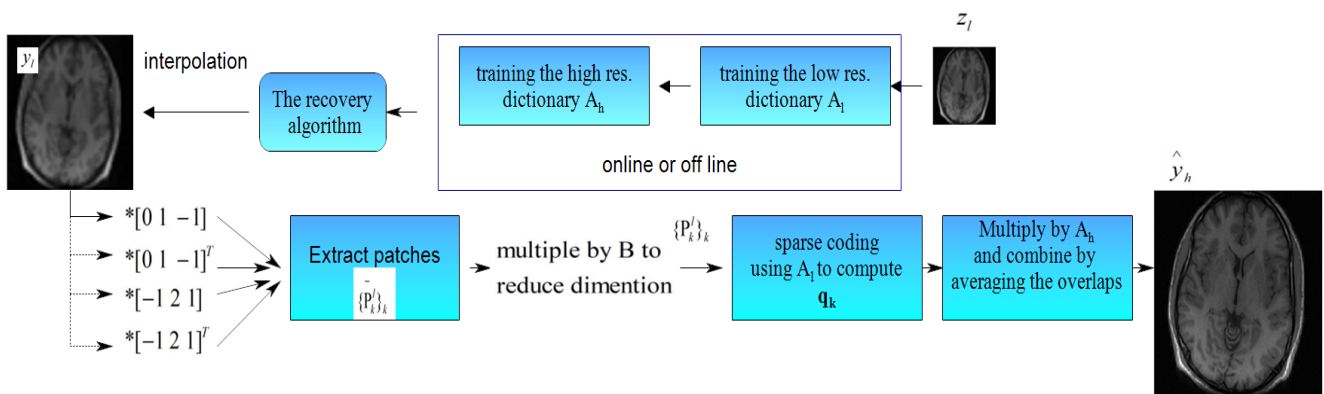Figure 6. Refinement of an interpolated high resolution image (by Bicubic interpolation) for Super Resolution

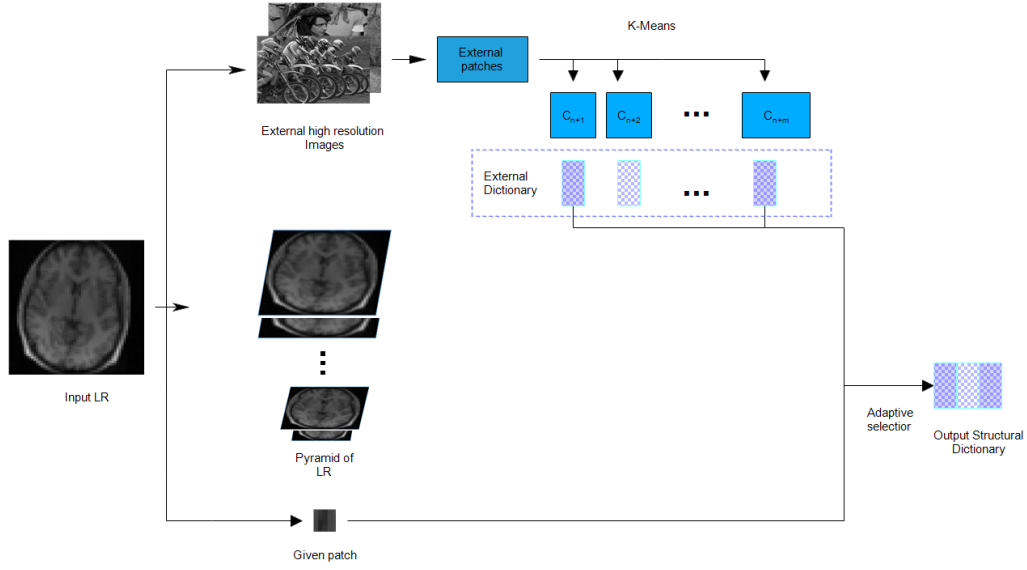Figure 7.The super-resolution algorithm used in the proposed method

Figure 8. The flowchart diagram of the algorithm for Image Deblurring and Super-resolution by Adaptive SparseDomain Selection and Adaptive Regularization (ASDS)

Table1. The description of the symbols used in this paper

Symbol		description	
y_h	vector of length N_h pixel	y_l	scaled up image
$\mathbb{H}$	The blur operator	P_h^k	high-resolution image with $\sqrt{n} \times \sqrt{n}$ patch size
z_l	low-resolution and noisy image	v	additive white Gaussian noise
k	pixels locations/number of clusters	s	Scale factor
A_h, A_l	high-/low- resolution dictionaries	Q	Bicubic interpolation operator
L_{all}	degrading operator	q^k	sparse representation vector
ϕ_{k_i}	orthogonal sub-dictionaries	x_i	vector image
R_i	a matrix extracting patch x_i	x	reconstructed image
S_h	high pass filter	Λ_k	coefficient matrix
P_k	orthogonal transformation matrix	$\alpha_{i,j}$	coefficient related to j^{th} atom of ϕ_{k_i}
$\lambda_{i,j}$	weight dedicated to $\alpha_{i,j}$		

Table2. The average running time of different methods

Method	PMRI	ASDS-TD1	ASDS-AR-TD1	ASDS-AR-NL-TD1	Bicubic	Proposed Method	ASDS-TD2	ASDS-AR-TD2	ASDS-AR-NL-TD2
Running time(s)	180	728	740	780	45	**30**	483	545	666

Table3. Psnr(DB), SSIM and RMSE results

Method / MRI image	ASDS-TD1	ASDS-AR-TD1	ASDS-AR-NL-TD1	Bicubic	Proposed Method	ASDS-TD2	ASDS-AR-TD2	ASDS-AR-NL-
Psnr	30.90	31.42	31.46	30.0206	**33.1133**	32.02	32.13	32.3023
SSIM	0.716	0.8532	0.8741	0.863	**0.8984**	0.8806	0.8812	0.8833
RMSE	8.1	8.8446	8.8435	6.31	**5.1459**	8.8773	8.56	7.7662

$$psnr = 10\log_{10}\left(\frac{255^2.N}{\sum_i (\hat{y}_i - y_i)^2}\right) \qquad (10)$$

The average running time of different methods is listed in Table 2. The PSNR, SSIM and RMSE results from different methods are listed in Table 3. For the proposed method, psnr calculated about 33. 1133db. The highest psnr value for the validation methods belongs to ASDS-AR-NL-TD2 (32.3023db). Training dataset 2 always had better results. From the visual comparison, it is obvious that the proposed method means combining pMRI and training both high- and low-resolution dictionaries to provide a better result (about 0.8111db difference in psnr). The proposed method for deblurring and super-resolution had much better visual results than bicubic interpolation. The validation algorithms are shown in Figure 11(a-g). Figure 10 represents the result of pMRI as an input image. Figure 11(a) represents the bicubic interpolation result, this interpolation was not able to remove the blur; As seen, the image is very smooth and it failed to reconstruct sharp edges. This method only uses weighted averaging on neighboring elements without considering the image degradation procedure; thus, it cannot recover high-frequency details of high-resolution images. Figure 11(b, c, d) represent that ASDS-TD1, ASDS-AR-TD1, ASDS-AR-NL-TD1 generate some artifacts in smooth regions, the edges are relatively smooth and some fine image structures are not recovered. It is obvious that the proposed method has fewer artifacts, it suppresses the noise, sharpens the edges with improved psnr as well as it is much faster because of K-SVD and OMP implementation. Many noise residuals and ghost artifacts in the deblurring image still exist after using the validation methods (ASDS-TD2, ASDS-AR-TD2, ASDS-AR-NL-TD2) as represented in Figure11(e, f, g). The proposed dictionary learning method was implemented on natural images. The best result belonged to the bmp type of natural images. By using pMRI on the complex double type and transmitting through wavelet and Fourier domain as well as choosing K-SVD algorithm instead of a lasso for training the high-resolution dictionary, it is capable of handling complex data as well. The proposed algorithm increased the number of image unit's representation. Therefore, the distance between the gray and white matters improves (Figure 11(h)).

Figure 9. The two datasets of high-quality images used for training sub-dictionaries. The first row represents the images of training dataset 1 and the second one represents the images of training dataset 2
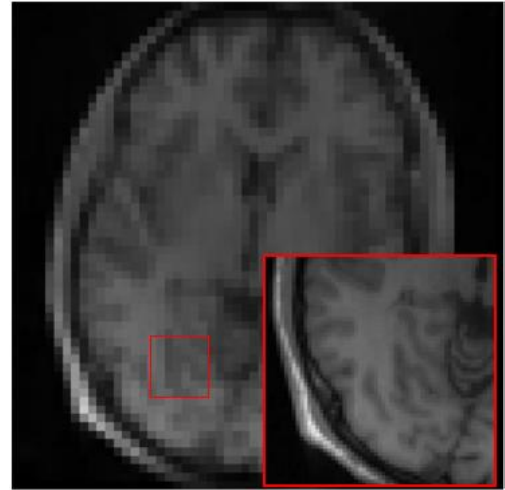

Figure 10. The result of pMRI reconstruction

6.1. Error image

A high-resolution ground truth image similar to the input image is required for obtaining the error image. Due to a lack of access to such an image, we assumed the reconstructed image (the result of the proposed method) to be the ground truth (Figure 12(a)). Figure (12(b)) represents the Error image of ASDS-AR-NL-TD2 and Figure(13(a)) is the pMRI result (input image). The error image of the proposed method (Figure 13(b)) contains less brightened white pixels. This approves that the proposed method contains less error.

7. Conclusion

Various methods used for image super-resolution and deblurring based on sparse representation and dictionary learning. For the first time, we combined pMRI and dictionary learning for super-resolution and deblurring of images in the complex double format. We used pMRI results as the test image for deblurring. For enhancing the scanning time of MR images, one efficient way is to acquire data from parallel multi-channel coils. The scanning time will significantly reduce if each coil acquires a small fraction of the whole measurement. Therefore, the procedure is less troublesome for the patient. The goal of this method, called pMRI, was to reconstruct the original image precisely. We deblurred the result of pMRI with sparse representation modeling and dictionary learning based on assuming a local *Sparse-Land* model on image patches, serving as regularization. The algorithm operated by training a pair of low- and high-resolution dictionaries, using the test images as the training dataset. Then, we evaluated our work with another single image super-resolution and deblurring algorithm that would use an adaptive sparse domain selection (ASDS) and adaptive regularization (AReg). This was because the optimal sparse domains of natural images would change significantly across different images and different image patches in a single image.
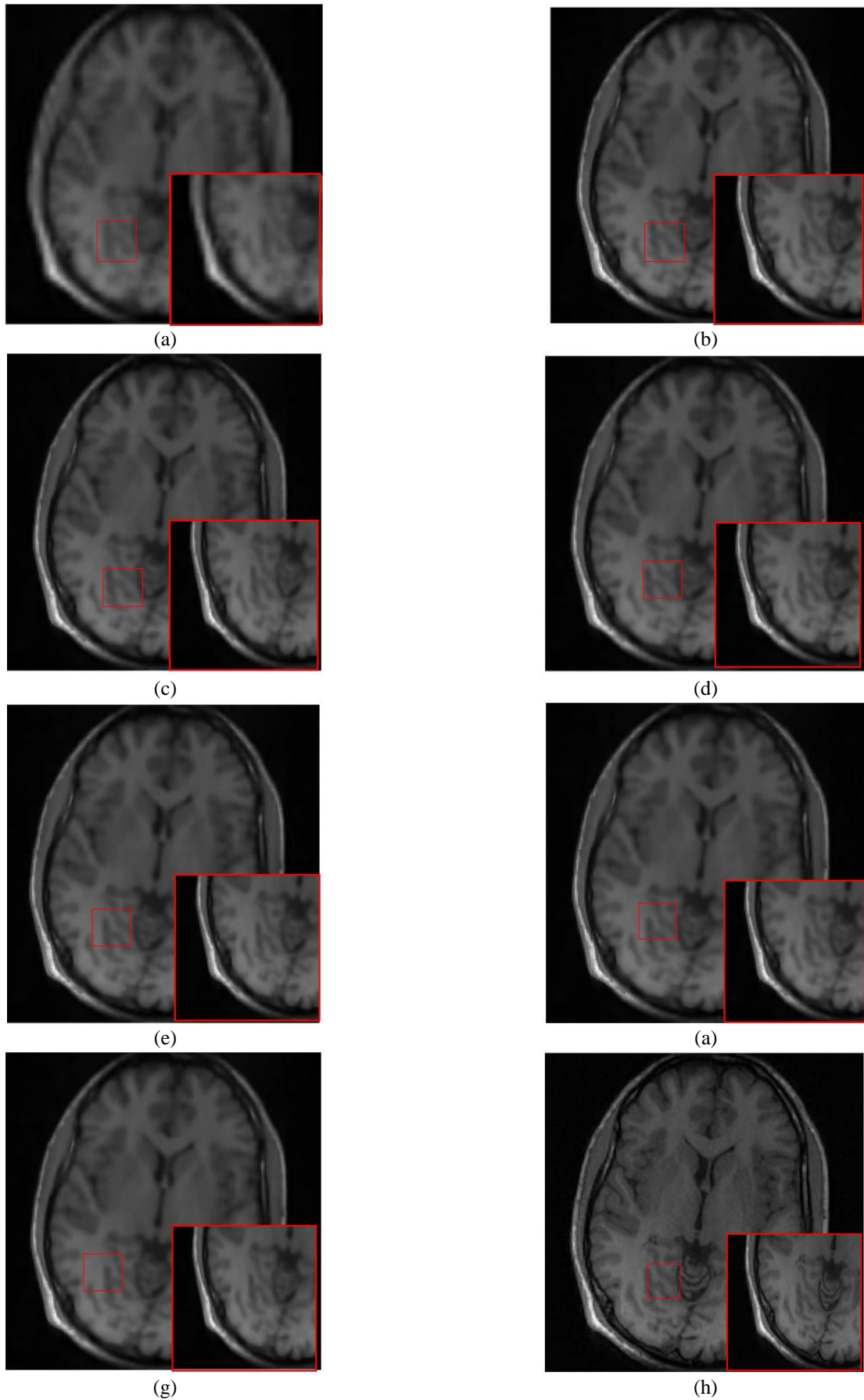
Figure 11. (a) Bicubic interpolation, (b) ASDS-TD1, (c) ASDS AR- TD1, (d) ASDS-AR-NL-TD1, (e) ASDS-TD2, (f) ASDS-AR-TD2, (g) ASDS-AR-NL-TD2, (h) Proposed method
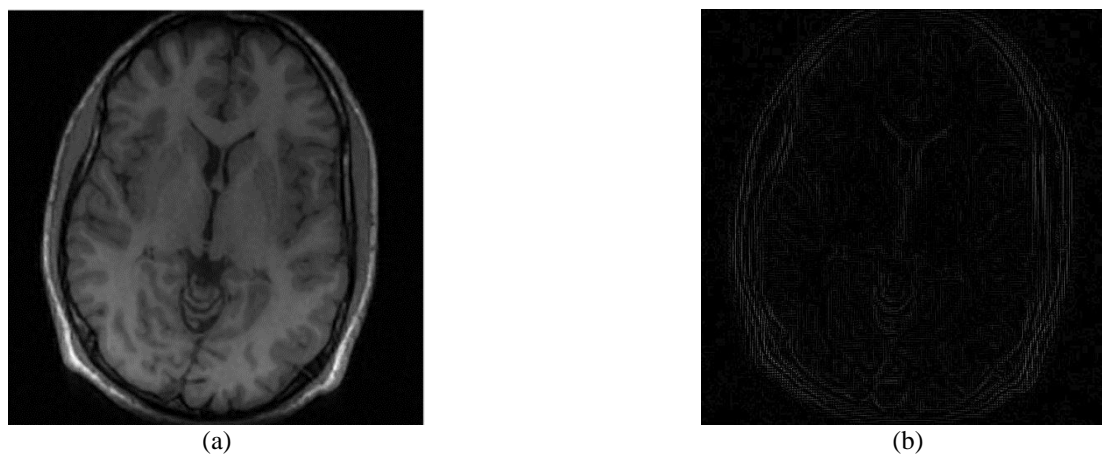
(a)   (b)

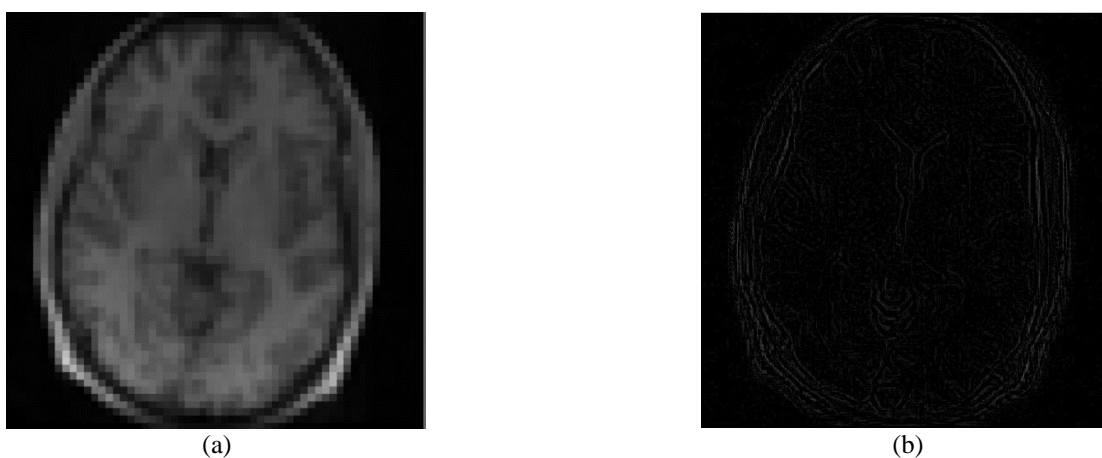Figure 12. (a) Ground truth, (b) The error image of ASDS-AR-NL-TD2

(a)   (b)

Figure13. (a) pMRI result (input image), (b) The error image of the proposed method

The experimental results showed that the proposed method was highly efficient in reducing ringing artifacts, suppressing noise, reconstructing sharper edges, and it was also much faster.

A different training approach was used for the dictionary-pair: K SVD for learning A_l from extracted features, and pseudo-inverse for A_h from error patches. The OMP algorithm was used as a sparse coding algorithm, which was much faster than l_1-optimization-based methods. Using two dictionaries (high and low) might improve the result of image super-resolution and deblurring By using different methods for the learning step, the algorithm was capable of handling complex data as well. Besides, the best approximation of $\left| \hat{y}_h - y_h \right|$ obtained while using different methods for learning high- and low-resolution dictionaries. It is possible to force the overlapping patches $\hat{P}_h^k$ to better align with each other. This can be carried out by operating sequentially on the incoming patches P_l^k, and when applying the sparse coding stage (to produce q^k), a penalty can be added on the distance between the newly constructed patch, $\hat{P}_h^k$, and the ones already computed.

References

Aharon, M., Elad, M, Bruckstein A.M. (2006) 'The K-SVD: An algorithm for designing of over complete dictionaries for sparse representation' IEEE Trans. on Signal Processing 54(11), 4311–4322.

Bertero, M., & Boccacci, P. (1998) 'Introduction to Inverse Problems in Imaging' pp 349-353.

Carlyle, S., Bushong, G. (2015) 'Magnetic Resonance Imaging Physical and Biological Principles., fourth edition, pp 44-48.

Chakraborty, A., Rajagopalan, A., & Chellappa, R. (2007) 'Super-resolution of face images using kernel pca-based prior' IEEE Transactions on Multimedia, 9(4), 888–892.

Chen, C., Huang, J. (2013) 'The benefit of tree sparsity in accelerated MRI' Medical Image Analysis,18(6),834-842.

Chen, C., Li, Y., & Huang, J. (2013) 'Calibration less parallel MRI with joint total variation regularization' Proceedings of the Annual International Conference on Medical Image Computing and Computer-Assisted Intervention (MICCAI), pp. 106-114.

Chen, C., Tian, F., Liu, H., & Huang, J. (2014) 'Diffuse optical tomography enhanced by clustered sparsity for

functional brain imaging' IEEE Transactions on Medical Imaging, 33(12), 2323-2331.

Dong, W., Zhang, L., Shi, G., & Li, X. (2013) 'Nonlocally centralized sparse representation for image restoration' IEEE Transactions on Image Processing, 22(4), 1620–1630.

Donoho, D. (2006) 'Compressed sensing' IEEE Trans. on Information Theory, 52(4), 1289-1306.

Elad, M., Figueiredo, M.A.T., & Ma Y. (2010) "On the Role of Sparse and Redundant Representations in Image Processing," Proceedings of IEEE, Special Issue on Applications of Compressive Sensing & Sparse Representation, June 2010.

Feinberg DA, Hale JD, Watts JC. (1986) 'Halving MR imaging time by conjugation: demonstration at 3.5 kG, Radiology; 161, 527-531.

Ferreira, J C. (2016) 'Algorithms for super-resolution of images based on sparse representation and manifolds'. Image Processing, fourth edition.

Ferreira, J. (2016) 'Algorithms for super-resolution of images based on sparse representation and manifolds' Image Processing [eess.IV]. Université Rennes 1..

Glasner, D., Bagon, S., Irani, M. (2009) 'Super-Resolution from a Single Image' International Conference on Computer Vision, ICCV, pp 349-356.

Glowinski, R., Osher, S. J., Yin, W. (2016) 'Splitting Methods in Communication, Imaging, Science, and Engineering' Springer, pp334-337.

He, L., Qi, H., & Zaretzki, R. (2013) 'Beta process joint dictionary learning for coupled feature spaces with application to single image super resolution' IEEE Conf. Computer Vision and Pattern Recognition, pp. 345–352.

Huang, D., Huang, Zh., Yuan, W., Zhang, J. (2018) 'image super resolution algorithm based on an improved sparse auto encoder' MDPI., 9(1).

Huang, J. (2011) 'Structured sparsity: Theorems, Algorithms and Applications' Ph.D. dissertation, Rutgers University.

Huang, J., Zhang, T., & Metaxas, D. (2009) 'Learning with structured sparsity' Proceedings of the International Conference on Machine Learning (ICML), pp. 417-424.

Huang, J.-B., Singh, A., & Ahuja, N. (2015) 'Single image super-resolution from transformed self-exemplars' IEEE Conference on Computer Vision and Pattern Recognition, pp 5197-5206.

Jiang, J., Hu, R., Wang, Z., & Han, Z. (2014) 'Noise robust face hallucination via locality-constrained representation' IEEE Transactions on Multimedia, 16(5), 1268–1281.

Kim, K.I. & Kwon, Y. (2010) 'Single-image super-resolution using sparse regression and natural image prior' IEEE Transactions on Pattern Analysis and Machine Intelligence, 32(6), 1127–1133.

Lee, CI., Haims, AH., Monico, EP., Brink, JA., Forman, HP. (2004) 'Diagnostic CT Scans: Assessment of Patient, Physician, and Radiologist Awareness of Radiation Dose and Possible Risks' Radiology ,231 (2),393-398.

Li, J., Liu, J., Pan.H Yao, J-S. (2017) 'magnetic resonance super resolution imaging measurement with dictionary-optimized sparse learning' measurement science review,17(3) ,145-152.

Li, Y., Chen, C., Axel, L., & Huang, J. (2014) 'Real time dynamic mri with dynamic total variation' Proceedings of International Conference on Medical Image Computing and Computer-Assisted Intervention (MICCAI). Springer,pp. 138-145.

Liang, D., Liu, B., Wang, J., & Ying, L. (2009) 'Accelerating sense using compressed sensing,' Magnetic Resonance in Medicine, 62(6),1574-1584.

Lustig, M., & Pauly, J. (2010) 'Iterative self-consistent parallel imaging reconstruction from arbitrary k-space' Magnetic Resonance in Medicine,64(2) , 457-471.

Marial, J., Bach, F., & Ponce, J. (2014) 'Sparse Modeling for Image and Vision Processing' Foundation and Trends in Computer Graphics and Vision, 8(2).

McGibney, G., Smith, M. R., Nichols, Crawley, S. T, A. (1993) 'Quantitative Evaluation of Several Partial Fourier Reconstruction Algorithms Used in MRI' Magn Reson Med, 30, 51-59.

Peng, Y., Ganesh, A., Wright, J., Xu, W., & Ma, Y. (2010) 'Robust alignment by sparse and low-rank decomposition for linearly correlated images' Proceedings of the IEEE Conference on Computer Vision and Pattern Recognition (CVPR), pp. 763-770.

Peng, Z., Chen, C., & Huang, J. (2014) 'O (1) algorithms for overlapping group sparsity' Proceedings of the International Conference on Pattern Recognition (ICPR). IEEE, pp. 1645-1650.

Pruessmann, K., Weiger, M., Scheidegger, M., Boesiger, P. (1999) 'SENSE: sensitivity encoding for fast MRI,' Magnetic Resonance in Medicine, 42(5), 952-962.

Reddy, D., Agrawal, A., & Chellappa, R. (2009) 'Enforcing integrality by error correction using 1-minimization' Proceedings of the IEEE Conference on Computer Vision and Pattern Recognition (CVPR), pp. 2350-2357.

Shields Health Care Group. (2010) 'Available from https://info.shields.com/bid/43435/MRI-CT-and-PET-Scan-Times'

Timofte, R., Smet, V. De, & Gool, L. Van. (2014) 'Adjusted anchored neighborhood regression for fast super-resolution' IEEE Asia Conf. Computer Vision, pp. 111–126.

Wang, J, Zhu, S., Gong, Y. (2010) 'Resolution enhancement based on learning the sparse association of image patches' Pattern Recognition Letters 31(1).

Williams LR.(2011) Lecture Notes for Computer Science 530, University of New Mexico, Available at http://www.cs.unm.edu/~williams/cs530/symmetry.pdf

Wright, J., Ma, Y., Mairal, J., Sapiro, G., Huang T. S., & Yan, S. (2010) 'Sparse representation for computer vision and pattern recognition' Proceedings of the IEEE, 98(6), 1031-1044.

Wright, J., Yang, A., Ganesh, A., Satyrs., & Ma, Y. (2009) 'Robust face recognition via sparse representation' IEEE Transactions on Pattern Analysis and Machine Intelligence, 31(2).,210-227.

Xiong, Z., Xu, D., Sun, X., & Wu, F. (2013) 'Example-based super-resolution with soft information and decision' IEEE Transactions on Multimedia, 15(6), 1458–1465.

Yang, J., Wright, J., Huang, T. S., & Ma, Y. (2010) 'Image super-resolution via sparse representation' IEEE Transactions on Image Processing, 19(11), 2861-2873.

Yang, J., Wright, J., Huang, T., Ma, Y. (2008) 'Image super-resolution as sparse representation of raw image patches',

IEEE Computer Vision and Pattern Recognition (CVPR). pp 1-8.

Yang, M.-C., Chu, C.-T., & Wang, Y.-C. F. (2010) 'Learning sparse image representation with support vector regression for single-image super resolution' IEEE International Conference on Image Processing, pp 1373-1376.

Zeyde, R., Elad, M., & Potter, M. (2011) 'On Single Image Scale-Up Using Sparse-Representations' International Conference on Curves and Surfaces, pp 711-730.

Zhang, L., & Wu, X. (2006) 'An edge-guided image interpolation algorithm via directional filtering and data fusion' IEEE Transactions on Image Processing15(8), 2226–38.

Zhang, L., Dong, W., Shi G, & Wu, X. (2011) 'Image deblurring and super-resolution by adaptive sparse domain selection and adaptive regularization', IEEE Trans. on Image Processing (TIP), 20(7), 1838-1857.

Zhu, Z., Guo, F., Yu, H., & Chen C. (2014) 'Fast single image super-resolution via self-example learning and sparse representation,' IEEE Transactions on Multimedia, 16(8), 2178–2190.